Title

Uncertainty Quantification of Unsteady Loading Noise of a Hovering Rotor Using Polynomial Chaos Expansion

Journal

Vertical Flight Society 81st Annual Forum and Technology Display

Authors

Gill, Hyunjune
Lee, Seongkyu

Publication Date

2025-05-20

DOI

10.4050/f-0081-2025-60

Uncertainty Quantification of Unsteady Loading Noise of a Hovering Rotor Using Polynomial Chaos Expansion

Hyunjune Gill
PhD Candidate

Seongkyu Lee
Professor

Department of Mechanical and Aerospace Engineering
University of California, Davis
Davis, California, 95616 U.S.A.

ABSTRACT

In this study, we employ Polynomial Chaos Expansion (PCE) to quantify the uncertainty of unsteady loading noise generated by a hovering rotor in the presence of a vertical gust. The unsteady loading noise is predicted using a frequency-domain approach combined with a quasi-steady blade element momentum theory, accounting for time-varying aerodynamic forces. A sinusoidal gust model, characterized by two parameters—gust length and gust amplitude—is introduced. Uncertainty quantification (UQ) of the unsteady loading noise is then performed using PCE based on these two gust parameters. The results show that the PCE method exhibits good agreement with the traditional Monte Carlo method. UQ analyses reveal that the largest uncertainty in unsteady loading noise occurs along the rotor axis. The individual and combined effects of the gust parameters on the acoustic uncertainty are analyzed, and parallel coordinate plots are employed to visualize parameter combinations that produce noise outliers or low noise levels. It is found that the gust length induces greater uncertainty in the unsteady loading noise than the gust amplitude, particularly at higher harmonics.

INTRODUCTION

Aeroacoustic noise prediction for hovering rotors is an essential aspect of rotorcraft design, particularly for applications in urban environments where noise regulations are becoming increasingly stringent (Refs. 1, 2). In an ideal hovering condition, the aerodynamic loads are assumed to be uniform and axisymmetric across the rotor disk, which allows steady loading models to sufficiently predict tonal noise. However, in reality, external factors, such as motor imperfections, inflow disturbances, rotor-airframe interactions, and atmospheric conditions introduce fluctuations in inflow velocity, leading to unsteady aerodynamic loads on the rotor blades.

Previous efforts have addressed the prediction of unsteady loading noise using various modifications to steady-state Blade Element Momentum Theory (BEMT). For instance, Kvurt and Stalnov (Ref. 3) introduced a method to model higher harmonic loads by assuming an arbitrary fluctuation rate based on steady-state loading information. Their approach demonstrated accurate noise predictions compared to experimental measurements. Additionally, Gill and Lee (Ref. 4) extended the classical BEMT to account for the variations in RPM and periodic fluctuations of vertical gusts. Despite the success of these methods, there remain uncertainties in the prediction of rotor acoustics due to factors such as the uncertain nature of external gusts.

Presented at the Vertical Flight Society's 81st Annual Forum & Technology Display, Virginia Beach, VA, USA, May 20–22, 2025.

To better address these uncertainties, the present study employs the Polynomial Chaos Expansion (PCE) method. The PCE approach allows for efficient quantification of uncertainty in aeroacoustic predictions by representing the random variables that influence unsteady loads, such as the shapes and sizes of vertical gusts. The goal of this work is to evaluate the unsteady loading noise generated by a hovering rotor under the influence of a vertical gust, where these sources of uncertainty can have a significant impact on the acoustic footprint of the rotor.

This paper primarily investigates the effect of a sinusoidal vertical gust on the unsteady loading noise of a rotor. Vertical gusts can occur due to perturbation in the atmospheric pressure at which a rotor is operating or influence by a surrounding structure. For instance, Fig. 1 illustrates one potential reason for the generation of vertical gusts on the rotor. A common drone or UAM configuration (Refs. 5–7) shows a placement of a strut or a wing directly under the rotor during hover, during which disturbances in vertical velocity can occur as the blade rotates over the strut or the wing. A change in vertical velocity can alter aerodynamic loads and can be a source of unsteady loading noise.

The focus is on quantifying the acoustic impact by gust parameters, such as gust length and amplitude, using quasi-steady BEMT and the PCE framework. It aims to provide a more comprehensive understanding of the acoustic behavior of hovering rotors in the presence of external disturbances on inflow. The results of this work will contribute to more accurate evaluations of the impact of rotor noise, which is

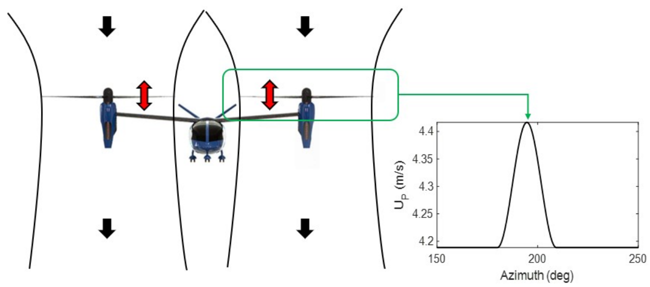

Fig. 1: One of potential reasons for vertical gust on a rotor.

crucial for the design of quieter rotorcraft, especially in the context of electric Vertical Take-Off and Landing (eVTOL) aircraft (Refs. 8, 9).

METHODS

Aerodynamic Model

In the case of a hovering rotor, classical methods such as BEMT provide only steady aerodynamic loads on the rotor disk, as they assume a uniform distribution of inflow velocity along the azimuth. Although this assumption is valid for rotor performance analyses, it limits the ability to perform realistic acoustic analysis of a hovering rotor. Previous steady frequency-domain approaches (Refs. 10–15) have indicated that tonal noise is inaudible along the rotor axis under hover and axial forward flight conditions. However, many experiments (Refs. 3, 16, 17) have shown that significant tonal noise is still detected along the rotor axis due to unsteadiness in the inflow velocity. To address these discrepancies, the quasi-steady application of BEMT has been presented by Gill and Lee (Ref. 4) to account for external influences on the inflow velocity passing through the rotor disk. This quasi-steady BEMT method equates azimuthally averaged sectional thrust at each radial location to determine the inflow velocity and, consequently, the thrust at each location.

The sectional thrust from blade element theory is given by:

$$dT = \frac{N_b}{2\pi}\int_0^{2\pi}\frac{1}{2}\rho U_T^2 c C_l \, dR \, d\psi \tag{1}$$

where N_b is the number of blades, ρ is the air density, U_T is the local tangential velocity, c is the chord length, C_l is the lift coefficient, dR is the differential radial element, and $d\psi$ is the differential azimuthal element in radians. The sectional thrust from momentum theory, without assuming a uniform inflow distribution, is given by:

$$dT = \int_0^{2\pi} 2\rho(V_c+v_i)v_i R \, dR \, d\psi \tag{2}$$

where V_c is, by definition, the climb or axial velocity at the rotor disk; however, the present study utilizes V_c to model vertical gust, and a method of modeling vertical gust is discussed in the subsequent paragraph. v_i is the inflow velocity. By equating Eq. (1) and Eq. (2), the perpendicular velocity (U_P) at any given location on the rotor disk can be derived as follows:

$$U_P(R,\psi) = \sqrt{\left(\frac{N_b c C_{l\alpha} U_T(R,\psi)}{16\pi F R} - \frac{V_c(R,\psi)}{2}\right)^2 + \frac{N_b c C_{l\alpha}\theta_p U_T(R,\psi)^2}{8\pi F R}} - \left(\frac{N_b c C_{l\alpha} U_T(R,\psi)}{16\pi F R} - \frac{V_c(R,\psi)}{2}\right) \tag{3}$$

where $U_P = (V_c + v_i)$. U_T and V_c are now functions of the blade radius (R) and the azimuth (ψ). $C_{l\alpha}$ is the lift-curve slope, F is Prandtl's tip and root loss function, and θ_p is the blade pitch angle. The non-dimensional form of Eq. (3) can be obtained by dividing both sides of the equation by ΩR_t, where R_t is the rotor radius. The resulting non-dimensional form for a rotor with rectangular blades is shown in Eq. (4) below:

$$\lambda(r,\psi,\lambda_c) = \sqrt{\left(\frac{\sigma C_{l_\alpha}}{16F} - \frac{\lambda_c}{2}\right)^2 + \frac{\sigma C_{l_\alpha}}{8F}\theta_p r} - \left(\frac{\sigma C_{l_\alpha}}{16F} - \frac{\lambda_c}{2}\right) \tag{4}$$

where $\lambda = \frac{U_P}{\Omega R_t}$, $\lambda_c = \frac{V_c}{\Omega R_t}$, and $\sigma = \frac{N_b c}{\pi R_t}$ for a rectangular-bladed rotor. This form is identical to the steady-state BEMT inflow ratio formulation, thus indicating that the aerodynamic loads are determined using the quasi-steady method.

A local thrust can be calculated using the following expression:

$$dT(R,\psi) = \frac{N_b}{4\pi}\rho U_T(R,\psi)^2 c C_{l\alpha}(\theta_p - \phi(R,\psi))dR \tag{5}$$

where N_b is the number of blades and $\phi(R,\psi)$ is the inflow angle. One of the advantages of this approach is that the tangential and vertical velocities can be modeled mathematically for simplicity or measured directly through experiments.

The present study considers the effect of the vertical gust on the unsteady loading noise. A gust modeling method as shown in Eq. (6) is adopted from Wang et al. (Ref. 18)

$$V_c(t) = \begin{cases} \frac{1}{2}V_p\left(1-\cos\left(\frac{2\pi(t-T_0)V_{\text{ref}}}{l_g}\right)\right) & T_0 < t < T_0 + l_g/V_{\text{ref}}, \\ 0 & \text{otherwise}, \end{cases} \tag{6}$$

where l_g is the gust length, V_p is the peak gust velocity, V_{ref} is a reference velocity obtained from 70% of the blade radius, T_0 is the time of gust onset, $t = \psi/\Omega$, and Ω is the rotation rate in radians per second. The resulting vertical velocity V_c in Eq. (6) is equivalent to the climb velocity V_c in Eq. (2) at a given time or azimuthal location.

Figure 2 shows an example of the modeled gust that a section of one blade experiences during its revolution. The black dashed lines indicate the onset (T_0) and end of the vertical gust in time, the distance between these dashed lines defines the gust length (l_g), and the red dashed line indicates the amplitude of the vertical gust (V_p). Since the shape and size of the gust can be characterized by the gust length and amplitude, uncertainty quantification is carried out using these two parameters.

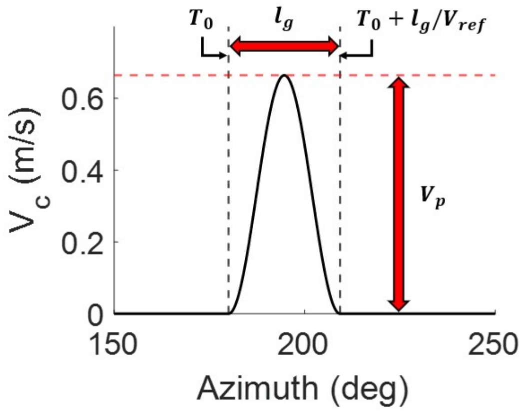

Fig. 2: An example gust modeled by Eq. (6).

Figures 3(a) and 3(b) illustrate the perpendicular velocity (U_P) and the thrust distribution on the rotor disk, respectively, after including the modeled gust. The black circles on the contour plots indicate the 70% of the rotor radius where the sectional thrust is determined, as shown in Fig. 3(c). Introducing a vertical gust at approximately 200 degrees of azimuth increases the magnitude of perpendicular velocity going through the rotor disk, which reduces the angle of attack. This reduction in angle of attack consequently decreases thrust at this location. The disturbance caused by the gust is assumed to affect the entire blade section. In other words, the gust modeling is incorporated in all radial sections of the blade. The simulation of the unsteady aerodynamic performance of a rotor is based on an experiment by Kvurt and Stalnov (Ref. 3), which utilizes the operating condition as shown in Table 1.

Table 1: Operating condition of Mejzlik heavy duty (HD) rotor (Ref. 3).

N_b	Radius (m)	RPM	Obs. Distance (m)
3	0.3556	1500	1.5

Aeroacoustic Model

Goldstein's frequency-domain tonal noise model (Ref. 15) was selected to analyze the unsteady loading noise of a hovering rotor due to its ability to rapidly predict loading noise in the presence of unsteady inflow distributions. Without delving into the detailed derivations, the final formulation of the model is provided as follows:

$$c_{mB} = \frac{imB^2\Omega}{4\pi a S} e^{i\frac{mB\Omega S}{a}} \sum_{\lambda=-\infty}^{\infty} e^{i(mB-\lambda)(\psi'-\pi/2)} \int_{hub}^{tip} \left[\cos\theta \frac{dT}{dR}\Big|_{\lambda} - \frac{a(mB-\lambda)}{mB\Omega R}\frac{dD}{dR}\Big|_{\lambda}\right] \times J_{mB-\lambda}\left(\frac{mB\Omega R}{a}\sin\theta\right) dR \tag{7}$$

where m is the acoustic harmonic index, λ is the loading harmonic index, B is the number of blades, a is the speed of sound, Ω is the rotation rate in radians per second, S is the observer distance from the rotor hub, $\psi' = \cos^{-1}(z/Y)$ is the in-plane observer angle, and θ is the observer angle from the rotor axis. Figure 4 illustrates the coordinate system used for rotor orientation and observer location in the acoustic analysis.

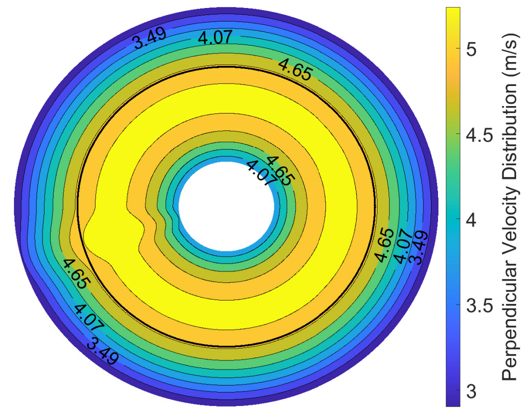

(a)

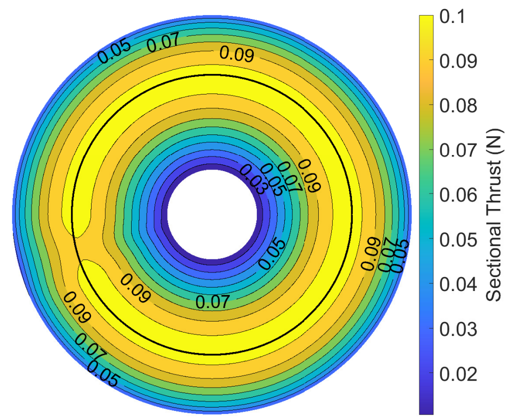

(b)

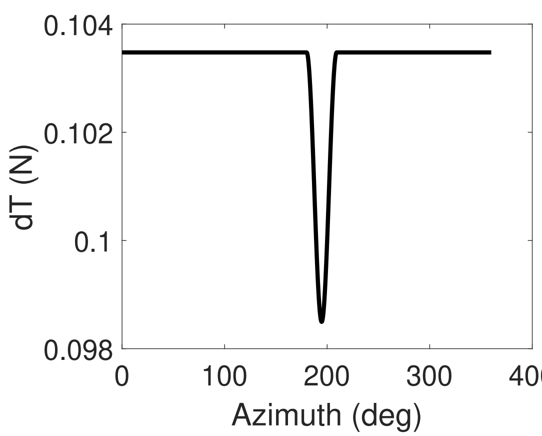

(c)

Fig. 3: (a) Perpendicular velocity distribution on the rotor disk, (b) thrust distribution on the rotor disk, and (c) sectional thrust at 70% of the rotor disk.

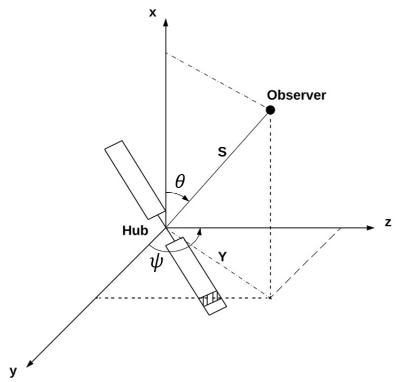

Fig. 4: Coordinate system used for the acoustic analyses.

The key aerodynamic inputs from the aerodynamic solvers are $\frac{dT}{dR}\big|_\lambda$ (sectional thrust) and $\frac{dD}{dR}\big|_\lambda$ (sectional drag). The temporal history of loads at each radial section, computed from the modified BEMT, is transformed into the frequency domain using a Fourier series, given by:

$$\frac{dT(R,\psi)}{dR} = \sum_{\lambda=-\infty}^{\infty} \frac{dT}{dR}\Big|_\lambda e^{i\lambda\psi} \tag{8}$$

It is important to note that a compact source assumption is made in this version of Goldstein's model. In the original model, chordwise non-compactness was considered in the aerodynamic load inputs to account for the retarded time variation along the chord of each blade section. However, the modified BEMT does not consider the chordwise variation of the aerodynamic loads.

It is worthwhile noting that this paper focuses only on tonal noise. Although broadband noise is important for small and large rotors (Refs. 19–23), this noise is not considered in this paper.

Uncertainty Quantification Analysis: Polynomial Chaos Expansion (PCE)

PCE is a method for uncertainty quantification that approximates the probability density function (PDF) of input parameters using a series of polynomial functions. For instance, the PDF of the input parameters can be approximated using Eq. (9), where X represents the input uncertainty parameters, such as the vertical gust amplitude or gust length. In this formulation, c_i represents the coefficient, and Ψ_i is the stochastic basis function (polynomials). The coefficients can be determined using the definition provided in Eq. (10), which is a general form of PCE for the input parameters X.

$$X \approx \sum_{i=0}^{p} c_i \Psi_i(\boldsymbol{\xi}), \quad X: \{V_p, l_g\} \tag{9}$$

$$\begin{aligned} c_i &= \frac{1}{\Psi_i^2}\int_\Omega X\Psi_i(\xi)\rho(\xi)d\xi \\ \Psi_i^2 &= \frac{\int \chi(\xi)\Psi(\xi)\rho(\xi)d\xi}{\int \rho(\xi)\Psi^2(\xi)d\xi} \end{aligned} \tag{10}$$

Table 2: Range of input uncertainty parameters drafted to select the mean values of the parameters.

Input Uncertainty Parameters	Range
Peak Gust Amplitude (V_p)	0.266 – 1.063 m/s
Gust Length (l_g)	0.05 m – 0.2 m

where p is the order of polynomial truncation, ρ is the PDF of the random variable, and $\chi(\xi)$ is the transformed random variable ξ to reflect the space of the PDF. For instance, if the input parameters and a function of random variables are normally distributed with a mean of 0 and standard deviation of 1, the random variable can be represented as

$$\begin{aligned} &\xi \sim N(0,1) \quad \text{with} \quad \rho(\xi) = \frac{1}{\sqrt{2\pi}} e^{-\frac{\xi^2}{2}} \\ &\chi(\xi) \sim N(M_N, S_N) \\ &\chi(\xi) = S_N\xi + M_N \end{aligned} \tag{11}$$

where M_N and S_N are mean and standard deviation of the normal distribution. The ranges of input uncertainty parameters are drafted as shown in Table 2 to select the mean values of the parameters that could represent realistic scenarios. These ranges are selected based on the feasibility of the strength and size of a gust potentially occurring in experimental settings or in-flight operations. For instance, the peak gust amplitude is specified to range between 0.266 and 1.063 m/s. These values correspond to 5 and 20% of the induced velocity at steady state, respectively. The gust length is expected to be 0.05 to 0.2 m which is equivalent to approximately 10 to 40 degrees of rotor azimuth. The median of these ranges are selected as the mean of the corresponding input uncertainty parameters. The standard deviation is determined using a metric called the coefficient of variation (CV), which is defined as $\text{CV} = S_N/M_N$, to quantify the uncertainty.

The stochastic basis function can be selected from the list provided in Table 3. These uncertain parameter types are represented by their corresponding orthogonal polynomials. Since the present study assumes a Gaussian distribution of uncertain parameters, the Hermite polynomial is selected as the stochastic basis function. The Hermite polynomial is represented by Eq. (12).

$$\Psi_i(\xi) = \text{He}_i(\xi) = (-1)^i e^{\frac{\xi^2}{2}} \frac{d^i}{d\xi^i} e^{\frac{-\xi^2}{2}} \tag{12}$$

Table 3: Types of uncertain parameters and the corresponding orthogonal polynomials.

Uncertain Parameter Type	Orthogonal Polynomials
Gaussian	Hermite
Gamma	Laguerre
Beta	Jacobi
Uniform	Legendre

A general form of PCE is as follows:

$$Y(\xi_1, \xi_2, ..., \xi_d) = \sum_{i \in \mathbb{I}_p} c_i \Psi_i(\xi_1, \xi_2, ..., \xi_d) \tag{13}$$

where Y is the output variable, ξ_d is the input random variable, c_i is the PCE coefficient for the corresponding index i, and Ψ_i is the stochastic basis function which is Hermite polynomial in the present study. The index i lies within the space $\mathbb{I}_p$ which represents the index set of all possible multi-indices that satisfy the total-degree truncation condition. For example, if the total-degree truncation condition is given by $p = 2$ for a two-variable (ξ_1 and ξ_2) PCE, then the general form in Eq. (13) can be expressed as

$$Y(\xi_1, \xi_2) = \sum_{i+j=0}^{p=2} c_{ij} \Psi_i(\xi_1) \Psi_j(\xi_2) \tag{14}$$

where Y is the output polynomial, and the summation of indices, i and j, do not exceed $p = 2$. The total number of terms in the expansion can be determined by Eq. (15).

$$N = \frac{(p+d)!}{p!d!} \tag{15}$$

Since the third-degree truncation has been sufficient to obtain converged solution, the two-variable PCE with third-degree truncation as represented by Eq. (16) is used to quantify uncertainty of sound pressure level (SPL) arising from the uncertainty in the gust parameters.

$$\begin{aligned} \mathrm{SPL}(\xi_1, \xi_2) &= \sum_{i+j=0}^{p=3} c_{ij} \Psi_i(\xi_1) \Psi_j(\xi_2) \\ &= c_{00}(1) + c_{10}(\xi_1) + c_{01}(\xi_2) + c_{11}(\xi_1)(\xi_2) \\ &+ c_{20}(\xi_1^2 - 1) + c_{02}(\xi_2^2 - 1) + c_{21}(\xi_1^2 - 1)(\xi_2) \\ &+ c_{12}(\xi_1)(\xi_2^2 - 1) + c_{30}(\xi_1^3 - 3\xi_1) + c_{03}(\xi_2^3 - 3\xi_2) \end{aligned} \tag{16}$$

Following Eq. (15), there is a total number of 10 terms in the expansion of the third-degree truncated two variable PCE.

The roots of the polynomial one order greater than the degree of truncation and zero are chosen to be the collocation points where the actual output SPLs are determined. For example, since the third degree of truncation is chosen, the roots of the fourth-order Hermite polynomial including zero for each random variable are {-1.65,-0.52,0,0.52,1.65}. The combination of these collocation points for two random variables is shown in Table 4. In other words, for two input uncertain variables, a total of 25 simulations are required to quantify the uncertainty of the SPL, resulting in a 25-by-10 matrix to determine the PCE coefficients (c_{ij}). Equation (17) shows the matrix form of the output SPLs from the required simulations to determine the PCE coefficients. The rows of the 25-by-10 matrix indicate Hermite polynomials at each simulation count, and the columns indicate the Hermite polynomials with all combination of the random variables. Therefore, the PCE coefficients are determined from Eq. (17), using the SPL values obtained from 25 simulations.

Table 4: Combination of all collocation points to determine PCE output coefficients.

Simulation Counts	ξ_1	ξ_2
1	-1.65	-1.65
2	-1.65	-0.52
⋮	⋮	⋮
5	-1.65	1.65
6	-0.52	-1.65
7	-0.52	-0.52
⋮	⋮	⋮
24	1.65	0.52
25	1.65	1.65

$$\begin{bmatrix} \mathrm{SPL}_1 \\ \mathrm{SPL}_2 \\ \vdots \\ \mathrm{SPL}_{24} \\ \mathrm{SPL}_{25} \end{bmatrix} = \begin{bmatrix} 1 & \xi_1 & \xi_2 & \cdots & (\xi_1^3 - 3\xi_1) & (\xi_2^3 - 3\xi_2) \\ 1 & \xi_1 & \xi_2 & \cdots & (\xi_1^3 - 3\xi_1) & (\xi_2^3 - 3\xi_2) \\ \vdots & & & \cdots & & \vdots \\ 1 & \xi_1 & \xi_2 & \cdots & (\xi_1^3 - 3\xi_1) & (\xi_2^3 - 3\xi_2) \\ 1 & \xi_1 & \xi_2 & \cdots & (\xi_1^3 - 3\xi_1) & (\xi_2^3 - 3\xi_2) \end{bmatrix} \begin{bmatrix} c_{00} \\ c_{10} \\ \vdots \\ c_{30} \\ c_{03} \end{bmatrix} \tag{17}$$

Once the output PCE coefficients are determined from Eq. (17), any combination of the two random variables that are represented by the normal distribution can be inserted back into Eq. (16) to determine the output SPL. In doing so, the number of aerodynamic and aeroacoustic simulations required to quantify the acoustic uncertainties can be significantly reduced compared to the traditional Monte Carlo method. It should be noted that the output SPL in Eq. (16) indicates the SPL at a single observer location at one acoustic harmonic index. In other words, if one is interested in multiple acoustic harmonic noise or the noise at various observer locations, the PCE simulations must be repeated to obtain the PCE coefficients that correspond to the acoustic harmonic indices or the observer locations.

Uncertainty Quantification Analysis: Monte Carlo (MC)

Compared to the PCE method, the MC method requires simulations of aerodynamic and aeroacoustic solvers at all input parameters to evaluate the corresponding SPLs. The schematic of MC simulation is shown in Fig. 5. Based on the mean and standard deviation of the input parameters, the normally distributed input variables for aerodynamic simulation are extracted. These variables are used in the aerodynamic solver to determine the aerodynamic loads on the rotor disk, which are used in the acoustic solver to determine the SPL of the unsteady loading noise. A total of 500 iterations were performed for the MC simulations of the single-variable cases. For the two-variable uncertainty quantification using the MC method, 400 iterations were performed. Since this method requires evaluations of the outputs for all input uncertain parameters, the MC method can be time consuming.

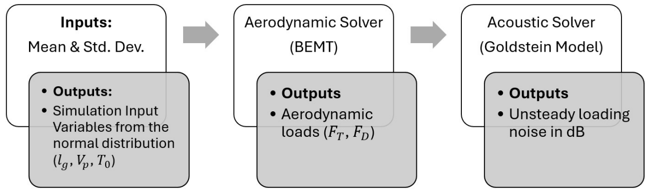

Fig. 5: Schematic of Monte Carlo simulation.

RESULTS

In this section, uncertainty quantification of three cases is presented: 1) acoustic impact due to gust length alone, 2) acoustic impact due to gust amplitude alone, and 3) acoustic impact due to combination of gust length and amplitude. Since the focus of this study is to quantify the uncertainties in the unsteady loading noise due to the uncertainties in the gust parameters, no direct comparison with the experimental data is presented.

Acoustic Impact due to Gust Length Alone

One characteristic of a gust that can induce unsteadiness in aerodynamic loads on a rotor disk is length of the gust. The gust amplitude is kept constant at its mean while performing uncertainty quantification analyses using the gust length. Figure 6 shows the uncertainty of the SPLs at multiple blade passing frequencies (BPFs) at various observer locations. $\theta = 0^\circ$ and 180° indicate the rotor axis, and $\theta = 90^\circ$ indicates the rotor plane. For all acoustic harmonics, the unsteady loading noise is the maximum at the rotor axis and the minimum at the rotor plane which aligns with the dipole nature of loading noise. The black dashed lines mark the minimum and maximum of SPLs obtained from the PCE simulation at each observer location, the solid black line indicates the mean SPL determined from the MC simulation, and the red dashed line indicates the mean SPL determined from PCE. The regions shaded in gray indicate the areas where the output uncertainty is present when the uncertainty in the gust length is introduced. The means from the MC and PCE simulations show good agreement at all observer locations as they overlap each other, which indicates that PCE with third-degree polynomial truncation is sufficient for converged solutions. At the first harmonic ($m = 1$), the SPL distributions at all observer locations are generally centered around the mean SPL. However, the rest of the harmonic cases show strong skewness at $m = 3$ and $m = 4$ or mild skewness at $m = 2$ and $m = 5$. At these harmonics, the mean SPLs are closer to the upper limit, which indicates that there is a higher probability that the gust length produces noise closer to the upper limit.

Furthermore, the largest distribution of the SPLs occurs at the rotor axis. This observation indicates that the acoustic magnitude at the rotor axis is more sensitive to unsteadiness in the aerodynamic loads. The mean and standard deviation along with the minimum and maximum of the output SPLs from the PCE simulations at $\theta = 0^\circ$ are summarized in Table 5. The largest mean SPL occurs at $m = 3$ but shows the smallest distribution of data about the mean, with the difference between the maximum and minimum being 2.4 dB. The largest distribution of data occurs at $m = 5$ with the difference between the maximum and minimum being 8.96 dB. It is important to note that this result is based on the input CV value of 0.10. This means that the standard deviation of the input parameter is 10% of the mean gust length.

Table 5: Means and standard deviations of unsteady loading noise of the first five harmonics at $\theta = 0^\circ$ (CV = 0.1) as a result of uncertainty in l_g.

Harmonic Index	$m = 1$	$m = 2$	$m = 3$	$m = 4$	$m = 5$
Mean	36.57	41.57	43.34	43.22	41.46
Std. Dev.	0.81	0.60	0.27	0.40	1.30
Minimum	33.12	38.90	41.18	39.73	34.62
Maximum	39.11	43.09	43.58	43.58	43.58

The distribution of the output SPLs is further analyzed at $\theta = 0^\circ$. The histogram in Fig. 7 shows the SPL distribution at $\theta = 0^\circ$ for the first five BPFs along with the fitted normal distribution curve in red. A normal distribution of SPLs is observed at $m = 1$ and a mild left skewness in the distribution at $m = 2$ and $m = 5$; however, a strong left skewness is present at $m = 3$ and $m = 4$. This result indicates that when an uncertainty in gust length is introduced, the highest mean SPL occurs at the 3rd and 4$^{\text{th}}$ BPF with a small uncertainty.

More CV cases are studied to observe how the uncertainty of the output SPLs responds to different distributions of the input parameter. CV indicates the amount of variation from the mean. For example, if CV equals 0.1, the standard deviation from a mean is 10% of the mean. Figure 8 shows the relationship between the CVs of the gust length and the CVs of SPL at $\theta = 0^\circ$. The increase in the SPL distribution with respect to the mean as the gust length distribution increases is most gradual at $m = 3$ and $m = 4$. The corresponding slopes of the linear fit between the input CVs and the output CVs are 0.0774 and 0.1125 at $m = 3$ and $m = 4$, respectively. This means that for every 0.1 increase in the CV of the gust length, there is a 0.0077 increase in the CV of 3$^{\text{rd}}$ BPF loading noise and a 0.0113 increase in the CV of 4$^{\text{th}}$ BPF loading noise. In other words, if the gust length varies between 0.1125 and 0.1375 m, the 3$^{\text{rd}}$ BPF unsteady loading noise that corresponds to the values of one standard deviation of the mean will vary between 43 and 43.67 dB, and similarly the unsteady loading noise at $m = 4$ will vary between 42.73 and 43.71 dB. For the same amount of increase in the gust length distribution, the distribution in the resulting SPL with respect to its mean increases more rapidly at $m = 5$ and the output CV is consistently higher than the rest of the acoustic harmonic cases. In other words, the uncertainty in the 5$^{\text{th}}$ harmonic SPL increases at a faster rate as the uncertainty in the gust length increases, and the highest uncertainty occurs at the 5$^{\text{th}}$ BPF. The CV slope at $m = 5$ is 0.3457, which means that if the gust length varies between 0.1125 and 0.1375 m, the 5$^{\text{th}}$ BPF unsteady loading noise that corresponds to one standard deviation of the mean are 40.03 and 42.89 dB. Then, two standard deviations of the mean SPLs are 38.59 and 44.33 dB.

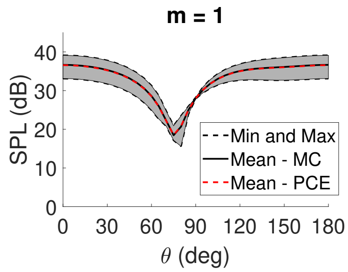

(a)

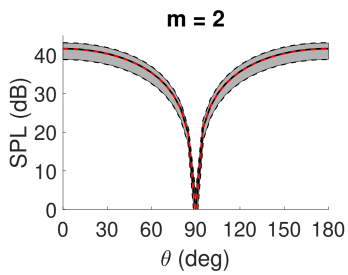

(b)

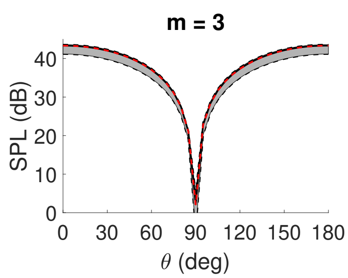

(c)

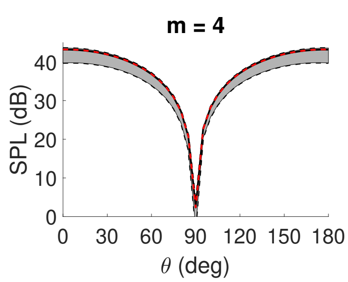

(d)

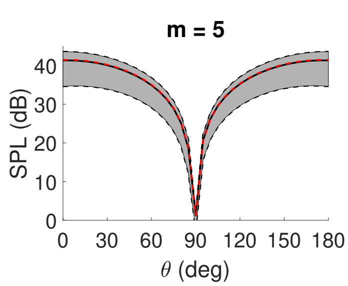

(e)

Fig. 6: Distribution of unsteady loading noise due to the uncertain quantity of gust length (l_g) at various observer locations (CV = 0.1): (a) 1st BPF noise, (b) 2nd BPF noise, (c) 3rd BPF noise, (d) 4th BPF noise, and (e) 5th BPF noise.

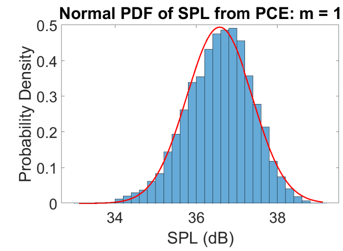

(a)

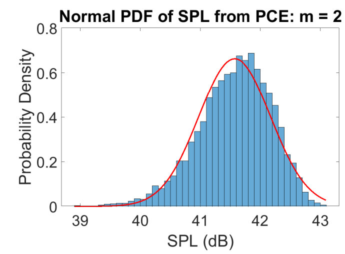

(b)

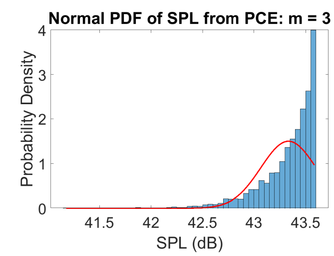

(c)

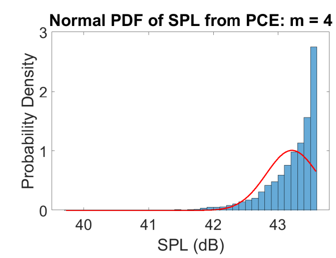

(d)

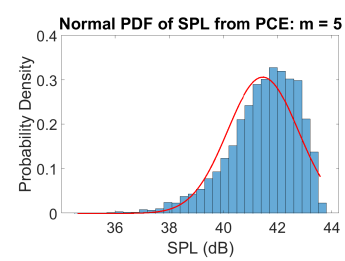

(e)

Fig. 7: Histogram and fitted normal probability density function (PDF) of the output SPLs at $\theta = 0°$ from PCE simulation as a result of uncertainty in gust length (CV = 0.1): (a) 1st BPF noise, (b) 2nd BPF noise, (c) 3rd BPF noise, (d) 4th BPF noise, and (e) 5th BPF noise.

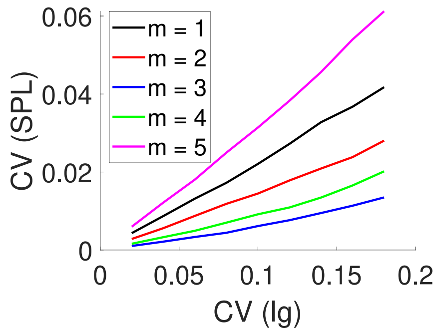

Fig. 8: Relationship between the coefficient of variation of the output SPL and the coefficient of variation of the input gust length at $\theta = 0^{\circ}$.

Table 6: Means and standard deviations of unsteady loading noise of the first five harmonics at $\theta = 0^{\circ}$ (CV = 0.1) as a result of uncertainty in V_p.

Harmonic Index	$m = 1$	$m = 2$	$m = 3$	$m = 4$	$m = 5$
Mean	36.60	41.58	43.37	43.30	41.63
Std. Dev.	0.89	0.89	0.89	0.90	0.92
Minimum	32.66	37.69	39.67	39.14	37.91
Maximum	39.27	44.17	46.35	45.89	44.62

Acoustic Impact due to Gust Amplitude Alone

Another characteristic of a gust that can induce unsteadiness in aerodynamic loads on a rotor disk is amplitude of the gust. For this analysis, the gust length is kept constant at its mean value. The directivity pattern in Fig. 9 is consistent with the previous case with only uncertainty in the gust length. The main difference between the current case and the previous case arises in the distribution of the output SPLs. As shown in Fig. 9, the means of the output SPLs are generally located at the center of the distributions at all observer locations. Notable differences in the distributions are observed at $m = 3$ and $m = 4$. When the gust length was varied in the previous case, the distribution was skewed left, thus having a higher concentration of data near the maximum; however, in the current case where the gust amplitude is the uncertain parameter, there is no skewness in the distributions.

The distribution of the output SPLs in Fig. 10 at $\theta = 0^{\circ}$ further suggests that there is no presence of skewness in the output data. The means and standard deviations along with the minimum and maximum values are summarized in Table 6. The standard deviations across all acoustic harmonic indices are relatively constant, but the mean values are different, and the smallest mean occurs at $m = 1$ and the largest occurs at $m = 3$. The difference between the maximum and minimum SPLs at each harmonic index shows no significant variation in the range of the output SPLs across the harmonic indices.

The relationship between the input CV and the output CV is shown in Fig. 11. At all acoustic harmonics, the CV of the output SPL has a linear relationship with the CV of the input gust amplitude. There is no significant difference in CV for the harmonics between $m = 2$ and $m = 5$, but the CV of the 1st harmonic SPL increases more rapidly than the CV of the

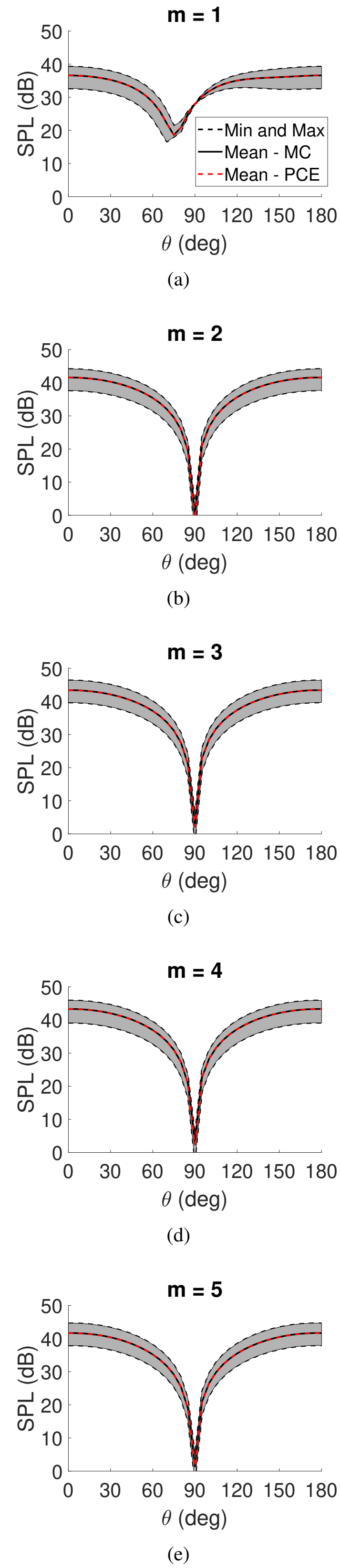

Fig. 9: Distribution of unsteady loading noise due to the uncertain quantity of gust amplitude (V_p) at various observer locations (CV = 0.1): (a) 1st BPF noise, (b) 2nd BPF noise, (c) 3rd BPF noise, (d) 4th BPF noise, and (e) 5th BPF noise.

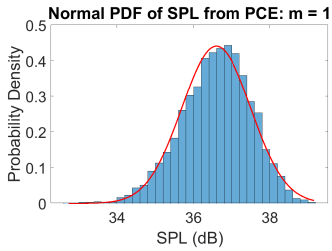

(a)

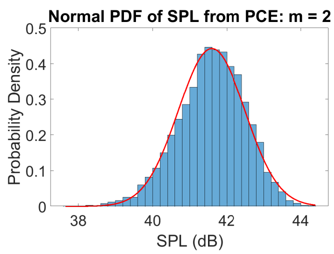

(b)

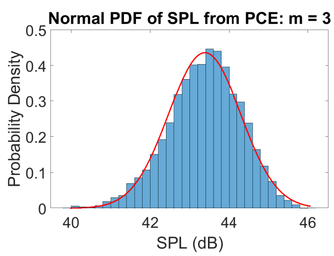

(c)

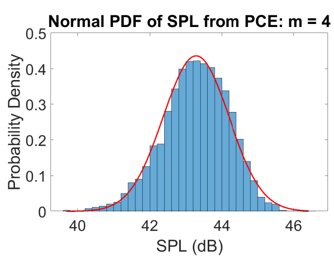

(d)

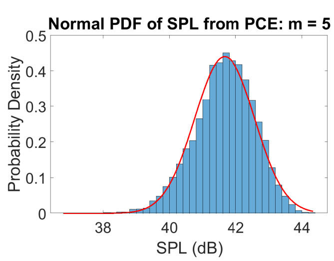

(e)

Fig. 10: Histogram and fitted normal probability density function (PDF) of the output SPLs at $\theta = 0°$ from PCE simulation as a result of uncertainty in gust amplitude (CV = 0.1): (a) 1st BPF noise, (b) 2nd BPF noise, (c) 3rd BPF noise, (d) 4th BPF noise, and (e) 5th BPF noise.

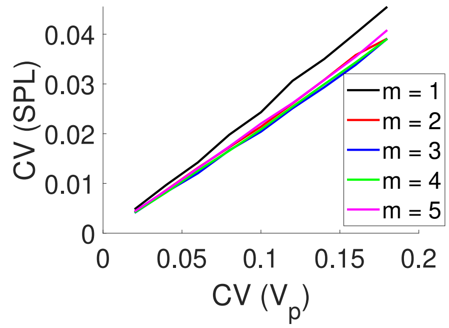

Fig. 11: Relationship between the coefficient of variation of the output SPL and the coefficient of variation of the input gust peak velocity at $\theta = 0°$.

other four harmonic SPLs. The slopes of the CVs of the 2nd through 4th BPF noise are relatively constant at 0.22, while the slope of the CV of the 1st BPF noise is 0.26. This means that for every 0.1 increase in the CV of the gust amplitude, the CV of the 1st BPF noise will increase by 0.026 and the CV of the higher harmonic noise will increase by 0.022. In other words, since the output SPLs show normal distribution, if the gust amplitude uncertainty is introduced with the standard deviation of 10% of the mean, there is 95% probability that the noise will be produced with a magnitude between 34.70 and 38.50 dB. Similarly, for the same gust amplitude uncertainty, there is 95% probability that the 2nd BPF noise will vary between 39.75 and 43.41 dB, the 3rd BPF noise will vary between 41.46 and 45.28 dB, the 4th BPF noise will vary between 41.39 and 45.21 dB, and the 5th BPF noise will vary between 39.80 and 43.46 dB.

Although the CV of the 1st harmonic SPL increases more rapidly, it does not indicate a greater uncertainty of the output SPL in this case since the mean values are different among the harmonic indices. Therefore, the distribution of SPLs with respect to the mean at each harmonic index is similar. In contrast, comparing Fig. 11 with Fig. 8 reveals that uncertainty in gust length introduces more uncertainty in the 5th harmonic SPL than the uncertainty in the gust amplitude does. Additionally, CVs of the 2nd through 4th harmonic SPLs increase more rapidly with increasing the CV of the gust amplitude than with increasing the CV of the gust length. Therefore, at these harmonics, the uncertainty in the SPL is more sensitive to the uncertainty in the gust amplitude.

Acoustic Impact due to Combined Gust Parameters

The uncertainties are introduced both in gust length and in amplitude. Figure 12 shows the uncertainty of the output SPLs as a result of the combined uncertainty in the input parameters at the observer locations between 0° and 180°. The mean of the PCE simulation aligns with the mean of the MC simulation, which indicates a sufficiently converged solution with the third-degree truncation for the two variable PCE analyses. Similar to the single uncertainty input parameter cases, the largest distribution of the unsteady loading noise occurs at the rotor axis for all acoustic harmonics. The distribution of the

Table 7: Means and standard deviations of unsteady loading noise of the first five harmonics at $\theta = 0°$ (CV = 0.1) as a result of uncertainty in V_p and l_g.

Harmonic Index	$m = 1$	$m = 2$	$m = 3$	$m = 4$	$m = 5$
Mean	36.47	41.36	43.36	43.39	41.31
Std. Dev.	1.15	1.11	0.84	0.88	1.54
Minimum	31.34	37.79	40.23	39.48	32.83
Maximum	40.22	44.53	45.07	45.24	44.95

output data for $m = 3$ and $m = 4$ resembles the distribution observed from the gust amplitude case since the mean SPLs are not close to the maximums. The distribution of the output data shown in Fig. 13 is relatively normal with the means and standard deviations shown in Table 7 for all acoustic harmonics at $\theta = 0°$. The minimum and maximum SPLs in Table 7 show that the largest range of uncertainty of 12.12 dB occurs at $m = 5$.

The relationship between the CV of the output SPL and the CV of the combined input parameters is shown in Fig. 14 for an observer location of $\theta = 0°$. Both CVs of the input gust length and amplitude are jointly increased from 0.02 to 0.18. The CV of the 5th harmonic SPL shows the most rapid increase (linear fit slope of 0.49) as the CVs of the input parameters increase, the CV of the 1st harmonic SPL being the second (linear fit slope of 0.33). Since the output SPL distributions are normal, if the uncertainty is introduced to both gust parameters with the standard deviations of 10% of their means, there is 95% probability that the 5th harmonic noise will be produced with a magnitude between 37.26 and 45.36 dB, and the 1st harmonic noise will be produced with a magnitude between 34.06 and 38.88 dB. Comparing Fig. 14 with both Figs. 8 and 11 shows that the uncertainty in the gust length contributes more to the uncertainty in the 5th harmonic noise than that of the gust amplitude. On the other hand, the uncertainties of the 2nd through 4th harmonic noise are more affected by the uncertainty of the gust amplitude than that of the gust length. The trend of the 2nd through 4th harmonics' CV generally resembles the trend observed in Fig. 11.

The boxplot in Fig. 15 further visualizes the distribution of the output SPL at $\theta = 0°$. The upper and lower vertical dashed lines that extrude from the blue box, also known as whiskers, represent the top and bottom 25% of the data, respectively, and the box represents 50% of the data with the red horizontal line being the median. The red plus signs indicate outliers based on the given data distribution. At $m = 1$ and $m = 5$, a large distribution of the output SPLs is observed since the whiskers extend to cover a wide range of output SPLs. The 1st harmonic noise data is more concentrated approximately at 36 dB, while the 5th harmonic noise data are concentrated approximately at 42 dB. The most amount of outliers are also observed at these harmonics. The 2nd harmonic noise data are approximately concentrated at 42 dB but have shorter whiskers, indicating a narrower distribution of the data. At $m = 3$ and $m = 4$, the median noise is shown to be the highest, and the 3rd and 4th harmonic noise show a small variation in acoustic magnitude as a result of the combined uncertainty in

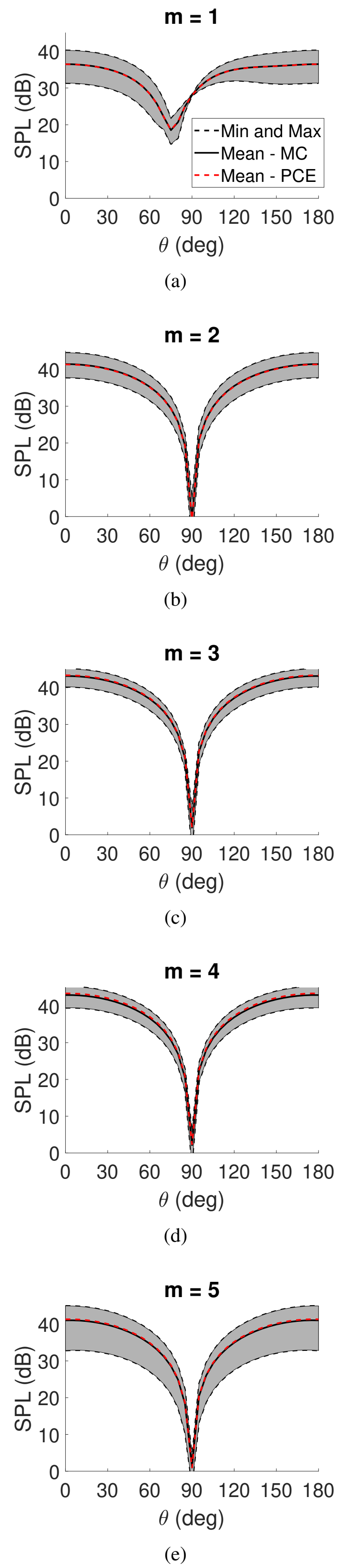

Fig. 12: Distribution of unsteady loading noise due to the uncertain quantities of gust length (l_g) and amplitude (V_p) at various observer locations (CV = 0.1): (a) 1st BPF noise, (b) 2nd BPF noise, (c) 3rd BPF noise, (d) 4th BPF noise, and (e) 5th BPF noise.

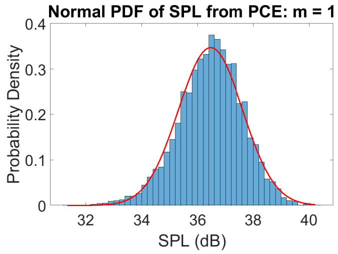

(a)

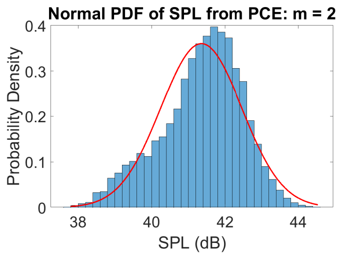

(b)

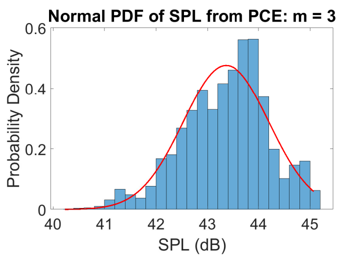

(c)

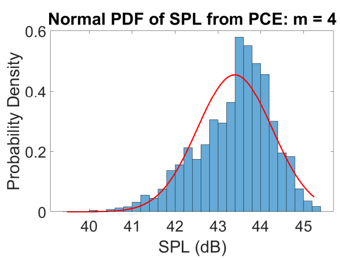

(d)

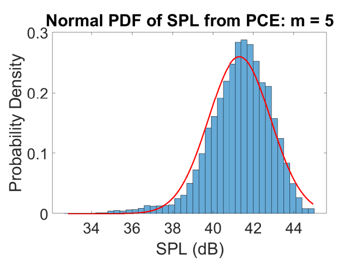

(e)

Fig. 13: Histogram and fitted normal probability density function (PDF) of the output SPLs at $\theta = 0°$ from PCE simulation as a result of uncertainty in gust length and amplitude (CV = 0.1): (a) 1st BPF noise, (b) 2nd BPF noise, (c) 3rd BPF noise, (d) 4th BPF noise, and (e) 5th BPF noise.

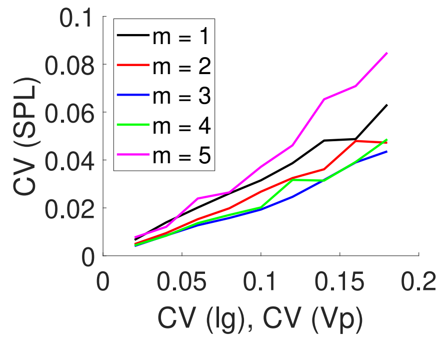

Fig. 14: Relationship between the coefficient of variation of the output SPL and the coefficient of variation of the input gust length and gust amplitude at $\theta = 0°$.

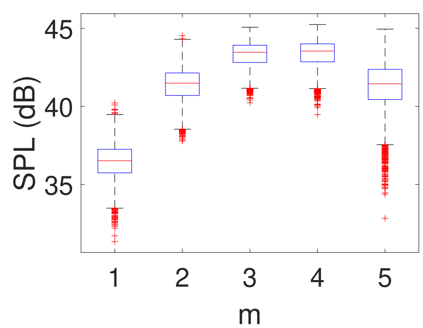

Fig. 15: Boxplots of the output SPLs for the first five BPFs at $\theta = 0°$.

the input parameters.

The outliers in Fig. 15 show the extreme ends of the data, and to observe a combination of input parameters that contribute to these extreme output SPLs, parallel coordinate plots (PCPs) are utilized. PCP is a tool that helps visualize all combinations of input parameters that lead to certain outputs of interest and helps trace back to the input parameters that contribute to those outputs of interest (Ref. 24). Figure 16 shows the PCPs in all five harmonics at $\theta = 0°$. The first two vertical axes on the left of Fig. 16 indicate the input parameters: gust amplitude (V_p) in m/s and gust length (l_g) in m. The third vertical axis shows the resulting output SPLs in dB. The gray lines show all combinations of input parameters that lead to output SPLs, and the red line shows all combinations of input parameters that lead to SPL outliers that are observed from Fig. 15. In this case, the SPL outliers are traced back to their origin to observe the combinations of input parameters that result in outliers. The lower outliers of the 1st through 3rd harmonic noise are generated by the low values of V_p and l_g. A combination of these two input parameters that are lower than their corresponding mean values (0.6441 m/s and 0.125 m, respectively) leads to the output SPL outliers. However, at the 4th harmonic, a combination between the lower-than-the-mean V_p with the higher-than-the-mean l_g leads to lower SPL outliers. At the 5th harmonic, lower SPL outliers are also generated even at higher V_p. This indicates that despite the higher gust amplitude, a combination with gust length can lead to the production of relatively low unsteady loading noise at a higher harmonic.

To further demonstrate the combination of the input parameters that lead to low unsteady loading noise production, the lowest 20% of the output SPLs are selected to trace back to the corresponding input parameters. The gray lines in Fig. 17 show all combinations of input parameters, while the red lines show the combinations of the input parameters that lead to the lowest 20% of the output SPLs. The results for the first three harmonics indicate that the low gust amplitude combined with narrow gust length leads to low noise; however, at higher harmonics like $m = 4$ and $m = 5$, the low gust amplitude combined with wider gust length leads to low noise. Conversely, it can also be concluded that the longer gust length produces a higher acoustic magnitude of unsteady loading noise at low frequencies, such as $m = 1$, 2, and 3, while the shorter gust length produces a higher acoustic magnitude at high frequencies such as $m = 4$ and 5.

CONCLUSION

Unsteady aerodynamic loads even under hover flight conditions have shown a significant contribution to loading noise, especially near the rotor axis. To capture this unsteady loading noise, the quasi-steady BEMT method was utilized in conjunction with Goldstein's frequency-domain tonal noise model. A sinusoidal gust was modeled to observe the effect of the gust parameters (gust amplitude and length) on unsteady loading noise. Uncertainty quantification was performed using MC and PCE methods. Comparison between the two methods showed good agreement and PCE's effectiveness despite the significantly smaller number of simulations that PCE required.

The acoustic impact due to the uncertain gust length was first analyzed. The distribution of the output SPLs showed strong left skewness at $m = 3$ and $m = 4$ with small uncertainty. Comparison between the CV of l_g and the CV of SPL revealed that the deviation from the mean was the largest at $m = 5$. The uncertainty of the 5$^{\text{th}}$ harmonic noise was more sensitive than that of the lower harmonic noise to the uncertainty in the gust length. With every 10% increase in the gust length uncertainty, 3.5% increase in the SPL uncertainty from the mean was observed.

Comparison with the gust length and amplitude cases at each harmonic showed that the uncertainty of the 5$^{\text{th}}$ harmonic noise was more sensitive to the uncertainty in the gust length alone, while the uncertainties of the 2$^{\text{nd}}$ through 4th harmonic noise were more sensitive to the uncertainty in the gust amplitude alone. With every 10% increase in the gust amplitude uncertainty, 2.2% increase in the SPL uncertainty from the mean was observed for the 2$^{\text{nd}}$ through 4$^{\text{th}}$ harmonics.

The uncertainty in the SPL due to the uncertainty of the combined gust parameters was also analyzed. With every 10% increase in the uncertainty of both gust parameters, 4.9% increase in the 5$^{\text{th}}$ harmonic SPL uncertainty from the mean was observed.

Using PCP, combinations of gust amplitudes and lengths that contributed to SPL outliers were traced. Another PCP was

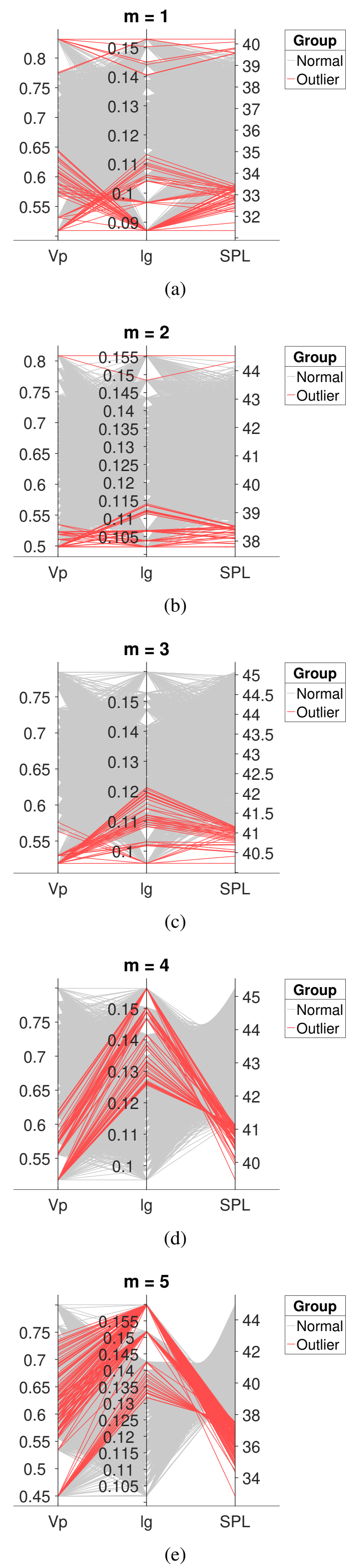

Fig. 16: Parallel coordinate plots of two input parameters (V_p and l_g) and one output parameter (SPL at $\theta = 0°$): (a) 1$^{\text{st}}$ BPF noise, (b) 2$^{\text{nd}}$ BPF noise, (c) 3$^{\text{rd}}$ BPF noise, (d) 4$^{\text{th}}$ BPF noise, and (e) 5$^{\text{th}}$ BPF noise.

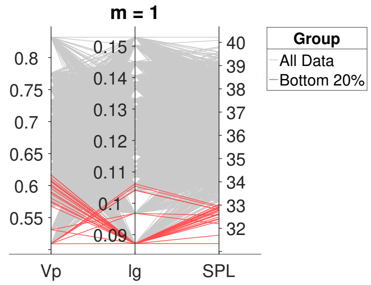

(a)

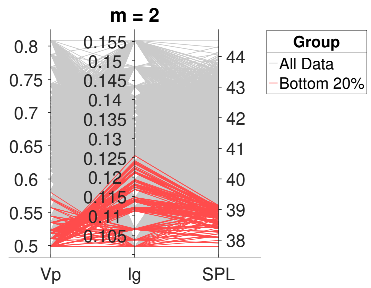

(b)

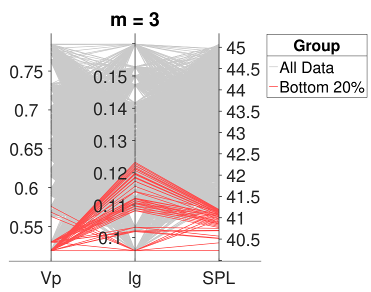

(c)

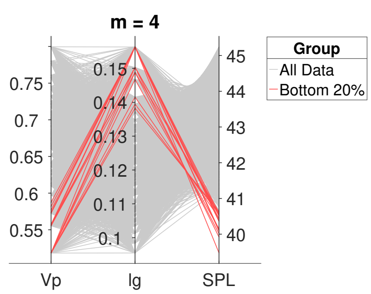

(d)

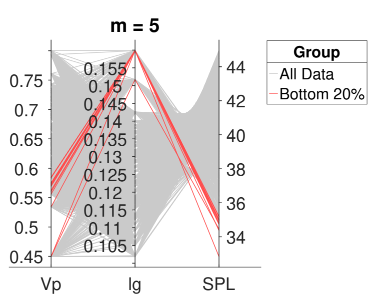

(e)

Fig. 17: Parallel coordinate plots of the combinations of V_p and l_g that lead to the lowest 20% of the output SPLs at $\theta = 0°$: (a) 1st BPF noise, (b) 2nd BPF noise, (c) 3rd BPF noise, (d) 4th BPF noise, and (e) 5th BPF noise.

generated to trace the combination of gust parameters that led to the lowest 20% of the output SPLs. Both results indicated that the generally low gust amplitude contributed to the low noise production at all harmonics. However, at a higher frequency, such as $m = 5$, low noise production was observed even at a high gust amplitude when combined with the longer gust length.

An underlying assumption in these statistical analyses of the acoustic impact due to gust characteristics is that unsteady aerodynamic effects are negligible, thereby justifying the use of quasi-steady BEMT. As part of future work, an unsteady aerodynamic model, such as the indicial response method, will be integrated into the uncertainty quantification framework to more accurately capture the effects of unsteady aerodynamics.

REFERENCES

[1] Sarojini, D., Ruh, M. L., Sperry, M., Yan, J., Fletcher, A., Joshy, A. J., Scotzniovsky, L., Ivanov, A., Orndorff, N., Gandarillas, V., Asher, I., Chambers, J., Gill, H., Lee, S., Cheng, Z., Rodriguez, G., Zhao, S., Mi, C., Nascenzi, T., Cuatt, T., Winter, T., Guibert, A., Cronk, A., Kim, A., Meng, S., and Hwang, J. T., "Large-Scale Multidisciplinary Design Optimization of an eVTOL Aircraft Using Comprehensive Analysis," *AIAA SciTech Forum*, AIAA Paper 2023–0146, Jan. 2023.
doi: 10.2514/6.2023-0146

[2] Ruh, M. L., Fletcher, A., Sarojini, D., Sperry, M., Yan, J., Scotzniovsky, L., van Schie, S. P. C., Warner, M., Orndorf, N. C., Xiang, R., Joshy, A. J., Zhao, H., Krokowski, J. J., Gill, H., Lee, S., Cheng, Z., Cao, Z., Mi, C., Silva, C., Wolfe, L., Chen, J. S., and Hwang, J. T., "Large-Scale Multidisciplinary Design Optimization of a NASA Air Taxi Concept Using a Comprehensive Physics-Based System Model," *AIAA SciTech Forum*, AIAA Paper 2024–0771, January 2024.
doi: 10.2514/6.2024-0771

[3] Kvurt, A. and Stalnov, O., "From the Blade Geometry to Prediction of Tonal Noise Component in Hover," Proceedings of the 28th AIAA/CEAS Aeroacoustics Conference, Southampton, UK, June 14–17, 2022, AIAA Paper 2022-3076.
doi: 10.2514/6.2022-3076

[4] Gill, H. and Lee, S., "Prediction of Rotor Unsteady Loading Noise in Hover Using an Unsteady Blade Element Momentum Theory," *AIAA SciTech*, AIAA Paper 2025–1043, Jan. 2025.
doi: 10.2514/6.2025-1043

[5] Radotich, M., "Conceptual Design of Tiltrotor Aircraft for Urban Air Mobility," Aeromechanics for Advanced Vertical Flight Technical Meeting, San Jose, CA, Jan. 25–27, 2022.

[6] Jia, Z. and Lee, S., "Computational Study on Noise of Urban Air Mobility Quadrotor Aircraft," *Journal of the American Helicopter Society*, Vol. 67, 2022, pp. 012009.
doi: 10.4050/JAHS.67.012009

[7]Sagaga, J. and Lee, S., "High-Fidelity Computational Study of Aerodynamic Noise of Side-by-Side Rotor in Full Configuration," *Journal of Sound and Vibration*, Vol. 592, 2024, pp. 118607.
doi: 10.1016/j.jsv.2024.118607

[8]Sarojini, D., Chambers, J. T., Wolfe, L., Doring, R., Despins, R., Ruh, M. L., Yan, J., Orndorff, N., Scotzniovsky, L., Xiang, R., Zhao, H., Krokowski, J. J., Chen, J.-S., Joseph, C., Anderson, R. M., Ning, A., Gill, H., Lee, S., Cheng, Z., Cao, Z., Mi, C., Cronk, A., Guibert, A., Kim, A., Meng, S., Silva, C., and Hwang, J. T., "Review of Computational Models for Large-Scale MDAO of Urban Air Mobility Concepts," AIAA SciTech, AIAA Paper 2024-0377, January 8–12 2024.
doi: 10.2514/6.2024-0377

[9]van Schie, S., Ruh, M., Fletcher, A., Warner, M., Sperry, M., Scotzniovsky, L., Orndorff, N., Xiang, R., Yan, J., Zhao, H., Krokowski, J., Chen, J., Sarojini, D., Gill, H., Lee, S., Tagg, A., Anderson, R., Green, E., Joseph, C., Ning, A., Cheng, Z., Cao, Z., Mi, C., Guibert, A., Cronk, A., Kim, A., Meng, S., Silva, C., and Hwang, J., "Large-Scale Distributed Multidisciplinary Design Optimization of the NASA Lift-Plus-Cruise Air Taxi Concept," AIAA SciTech Forum, AIAA Paper 2025-0362, January 6–10 2025.
doi: 10.2514/6.2025-0362

[10]Guttin, L., "On the Sound Field of a rotating Propeller," Technical Report NACA–TM–1195, National Advisory Committee for Aeronautics, October, 1948.

[11]Barry, F. W. and Magliozzi, B., "Noise Detectability Prediction Method for Low Tip Speed Propellers," Technical Report AFAPL–TR–71–37, Air Force Aero Propulsion Laboratory, June 1971.

[12]Hanson, D. B., "Influence of Propeller Design Parameters on Far-Field Harmonic Noise in Forward Flight," *AIAA Journal*, Vol. 18, (11), 1980, pp. 1313–1319.
doi: 10.2514/3.50887

[13]Lowson, M. V. and Ollerhead, J. B., "A Theoretical Study of Helicopter Rotor Noise," *Journal of Sound and Vibration*, Vol. 9, (2), 1969, pp. 197–222.
doi: 10.1016/0022-460X(69)90028-5

[14]Wright, S. E., "Sound Radiation from a Lifting Rotor Generated by Asymmetric Disk Loading," *Journal of Sound and Vibration*, Vol. 9, (2), 1969, pp. 223–240.
doi: 10.1016/0022-460X(69)90029-7

[15]Goldstein, M., "Unified Approach to Aerodynamic Sound Generation in the Presence of Solid Boundaries," *The Journal of the Acoustical Society of America*, Vol. 56, (2), 1974, pp. 497–509.
doi: 10.1121/1.1903283

[16]Brown, D. and Ollerhead, J. B., "Propeller Noise at Low Tip Speeds," Technical Report AFAPL–TR–71–55, Air Force Aero Propulsion Laboratory, September 1971.

[17]Whelchel, J., Alexander, W. N., and Intaratep, N., "Propeller Noise in Confined Anechoic and Open Environments," AIAA SciTech Forum, Orlando, FL, Jan. 6–10, 2020, AIAA Paper 2020–1252.
doi: 10.2514/6.2020-1252

[18]Wang, B., Warner, M., Tian, A., Scotzniovsky, L., and Hwang, J. T., "A Comparative Study of Uncertainty Quantification Methods in Gust Response Analysis of Lift-Plus-Cruise eVTOL Aircraft Wing," *arXiv*, Jan. 2025.
doi: 10.48550/arXiv.2501.03964

[19]Li, S. and Lee, S., "Prediction of Urban Air Mobility Multi-Rotor VTOL Broadband Noise Using UCD-QuietFly," *Journal of the American Helicopter Society*, Vol. 66, 2021, pp. 032004.
doi: 10.4050/JAHS.66.032004

[20]Lee, S., Ayton, L., Bertagnolio, F., Moreau, S., Chong, T. P., and Joseph, P., "Turbulent Boundary Layer Trailing-Edge Noise: Theory, Computation, Experiment, and Application," *Progress in Aerospace Sciences*, Vol. 126, 2021, pp. 100737.
doi: 10.1016/j.paerosci.2021.100737

[21]Li, S. and Lee, S., "Acoustic Analysis and Annoyance Assessment of a Quiet Helicopter for Air Taxi Operations," *Journal of American Helicopter Society*, Vol. 67, (3), 2022, pp. 1–15.
doi: 10.4050/JAHS.67.032001

[22]Gill, H. and Lee, S., "Development of a New Empirical Rotor Broadband Noise Prediction Models for Urban Air Mobility Applications," AIAA SciTech Forum, Orlando, FL, Jan. 8–12, 2024, AIAA Paper 2024–2473.
doi: 10.2514/6.2024-2473

[23]Li, S. and Lee, S., "Analytic Prediction of Rotor Broadband Noise with Serrated Trailing Edges with Applications to Urban Air Mobility Aircraft," *Journal of the American Helicopter Society*, Vol. 69, 2024, pp. 032005.
doi: 10.4050/JAHS.69.032005

[24]Khurana, M. and Yeo, H., "Uncertainty Quantification of the ONERA 7A Rotor Performance and Spanwise Structural Loads Using a Surrogate-Based Approach," *CEAS Acoustical Journal*, Vol. 15, 2024, pp. 933–956.
doi: 10.1007/s13272-024-00768-0